A molecular dynamics study of the energetics, diffusivities, and production of point defects in γU-Mo under applied pressure

Benjamin Beeler[a,b,], ATM Jahid Hasan[a], Gyuchul Park[c], Yongfeng Zhang[d,b], Shenyang Hu[e], Zhi-Gang Mei[c]

[a]Department of Nuclear Engineering, North Carolina State University, Raleigh, NC 27695, United States
[b]Idaho National Laboratory, Idaho Falls, ID 83415, United States
[c]Argonne National Laboratory, Lemont, IL 60439, United States
[d]Department of Nuclear Engineering and Engineering Physics, University of Wisconsin-Madison, Madison, WI 53706, United States
[e]Pacific Northwest National Laboratory, Richland, WA 99354, United States

Abstract

The United States High-Performance Research Reactor (USHPRR) program aims to convert Research and Test Reactors (RTR) from using high-enriched uranium (HEU) fuels to low-enriched uranium (LEU) fuels. A uranium-molybdenum (U-Mo) alloy of 10 weight percent Mo in a monolithic fuel foil and plate-type geometry is the primary design candidate for conversion. These fuel forms are bonded with a zirconium interdiffusion barrier to prevent interaction with the aluminum cladding. The design contains no plenum, and the fuel reaches very high levels of burnup, which can induce significant swelling and swelling-induced stresses in the fuel. The nature of how fundamental processes of radiation damage, including the evolution of point defects, occur under such stresses is unknown. In this work, we employ molecular dynamics simulations to investigate the formation energy, diffusion, and generation of point defects under applied stress. This work will allow for the implementation of stress-dependent microstructural evolution models of nuclear fuels, including those for both fission gas bubble growth and creep, which are critical to ensure the stable and predictable behavior of research reactor fuels.

1. Introduction

A monolithic fuel design with a uranium-molybdenum (U-Mo) alloy has been selected as the fuel for conversion in the United States High-Performance Research Reactor (USHPRR) program. This fuel design employs a U-Mo fuel foil bonded with a zirconium (Zr) interdiffusion barrier in aluminum (Al) cladding [1, 2]. This design increases the U density as compared to the current designs, allowing for a reduced enrichment of the fuel without a reduction in the achievable neutron flux, while removing the negative interaction growth regions in dispersion fuel [3]. An issue with U-Mo monolithic fuel is the large amount of swelling that takes place during operation [4]. Such swelling needs to be stable and predictable up to high fission densities, under variable temperature and power environments.

Research reactor fuels based on U-Mo operate up to very high levels of burnup, and can stably retain fission gases to high fission densities [5, 6, 7]. As such, there is a relatively high content of fission gas and

fission gas bubbles within the fuel matrix. The high number density and size of these bubbles can induce large localized stresses in the fuel [8, 9]. This large internal fuel pressure, combined with the Al cladding constraint and the fixed restraints at either end of the plate, results in a complex stress environment where relatively large compressive stresses are generated and in turn affect the microstructural evolution of the fuel. Finite element analyses have also observed localized regions of tensile stresses, due to the interaction of swelling, deformation, and regions of constraint [10]. One notable microstructural effect that is dependent upon this stress environment is the induced creep under irradiation, which has been observed experimentally [11] and explored preliminarily in a computational framework [12, 9].

Microstructural evolution can occur as a result of the accumulation of defects driven by short- and long-range interactions of microstructural features. A key input into creep models is the behavior of point defects under applied stress [8]. If the point defect formation behavior is modified due to a large local stress field, then the defect evolution, and thus the microstructural evolution, will be affected by that stress field. Mesoscale fuel performance simulations [13, 14, 15, 16] take into account information such as point defect formation energies and diffusion coefficients, in addition to creep behaviors, but typically assume an Arrhenius relationship that is independent of the stress state. Knowledge of the effects of stress on the fundamental nature of point defects will allow for the refinement of mesoscale evolutionary models and the parametrization of sophisticated creep models for U-Mo fuels. Elastic fields and the long-range elastic interaction between defects can be described via the elastic dipole and relaxation volume tensors [17, 18], and a first step towards obtaining these quantities is analysis of their energetics with and without applied load. Point defect formation energies and diffusion coefficients have been previously determined via molecular dynamics (MD) as a function of temperature and composition [19, 20, 21, 22], and the authors have conducted a preliminary study on the effects of pressure on point defect formation energies [23]. However, no studies on the effect of pressure on the diffusion of point defects have been conducted.

The generation of point defects in the fuel is also an area of limited study with regard to U-Mo fuels. There have been two studies on threshold displacement energies in metallic U [24, 25], one radiation damage study on γ-U [26], one radiation damage study on Mo [27] (with relevance to U-Mo fuels), and a few atomistic studies on radiation effects in the U-Mo alloy system [28, 29, 30]. Defect generation rates are also utilized as inputs into coupled cluster dynamics and phase-field models [31, 8] for the prediction of microstructural evolution. If applied stresses modify the rate of defect generation, then the subsequent defect accumulation and evolution will also be modified. The impact of applied pressure on defect generation is a topic that has not been thoroughly evaluated, but there exist prior studies showing statistically significant impacts of both tensile and compressive stresses in bcc Fe, Cu, and Fe-Cr [32, 33, 34, 35]. No such studies have been performed on U-Mo systems.

In this work, the effect of pressure on point defect formation energies, defect diffusion coefficients, and radiation damage in γU-Mo is investigated via MD. In addition, point defect formation volumes and elastic dipole tensors are reported.

2. Computational Details

MD simulations are performed utilizing the LAMMPS [..[1]][36, 37] software package and a U-Mo angular dependent potential (ADP) [20, 38]. This potential was fit to density functional theory data [..[2]]including multiple phases of U, Mo, and U-Mo, and reproduced *ab initio* reference data with the average accuracy of 281.97 meV/Å for the forces, 35.18 meV for the energies, and 4.2 kbar for the stresses, which is considered excellent agreement. The potential has been shown to reasonably [..[3]]predict a number of material properties and phenomena in both pure U and U-Mo alloys[..[4]], including phase stability/distortion [20, 43, 44], α-U diffusivity and grain boundary energetics [40, 41], and γU-Mo grain boundary properties [42]. Unfortunately, there are limited additional *ab initio* or experimental data available for further potential validation. However, in the authors' opinion, this potential is currently the most accurate tool for the description of the U-Mo phase in classical molecular dynamics.

2.1. Formation Energy, Formation Volume, and Dipole Tensor

A $14 \times 14 \times 14$ supercell consisting of 5,488 atoms is constructed in a body-centered cubic (bcc) structure, which is the relevant crystal structure for U-Mo research reactor fuels. Relaxation is performed in an *NPT* ensemble, relaxing each x, y, and z component individually, with a pressure damping parameter of 0.1 ps. A Nosé-Hoover thermostat is utilized with the temperature damping parameter set to 0.1 ps. Systems are investigated over a range of temperatures, from 600 to 1200 K in increments of 200 K. This temperature range was chosen due to the inherent properties of the potential, in that below 600 K γU becomes mechanically unstable and above 1200 K the crystal structure approaches the melting point. Further information on the structural stability of the γ phase and the role of chemical ordering on stability can be found in the literature [45, 46]. In this temperature range, all systems are verified to remain bcc in all simulations. Systems are relaxed for 100 ps, with volumes averaged over the final 50 ps. The equilibration is performed at a given pressure, ranging from -10 kbar to +10 kbar (-1 GPa to +1 GPa) in increments of 5 kbar. This pressure range should exceed any expected stress state of the fuel, and as such should present the possibilities of extreme behavior on defect evolution. Additionally, trends in behavior can be determined and explored at the pressures of interest. The sign of the pressure indicates compressive or tensile stress, in that a negative pressure applied to the supercell, results in tensile stress, while a positive pressure results in compressive stress. Eight individual compositions are investigated, including pure U and pure Mo, U-5Mo, U-10Mo, U-15Mo, U-30Mo, U-50Mo, and U-70Mo. All compositions are given in weight percent unless otherwise noted (for reference, these weight compositions correspond to 0, 12, 22, 30, 52, 71, 85, and 100 at.% Mo, respectively). This variation in composition allows for the analysis of a wide range of U-Mo systems, including all relevant compositions in monolithic fuel. During operation, the U-Mo system is expected to exist in the bcc

---

[1]removed: [36]
[2]removed: and
[3]removed: reproduce
[4]removed: [20, 39, 40, 41, 42].

Following the relaxation, the system is spatially scaled to the time-averaged volume as determined from the NPT simulation. A further relaxation of 50 ps is performed, the final 25 ps of which is utilized to determine average energies. A defect (vacancy or interstitial) is then inserted into the system and allowed to evolve for 50 ps, the final 25 ps of which is utilized to determine average energies. For an alloy composition, a proportional number of atoms are either removed or inserted, depending on the defect type, to closely maintain the stoichiometry of the system. For [..[5]]example, for an alloy of U-10Mo ($\approx$ 22 at.% Mo), 22% of the interstitials inserted are Mo atoms, while 78% of the interstitials inserted are U atoms. This allows for an exploration of an average defect behavior at a given concentration. For interstitials, an atom is randomly deposited into the supercell, provided that no other atom is within 1.5 Å, allowing for a random sampling of the entire supercell and all possible local configurational environments. To ensure statistical certainty of the results, 2000 simulations for each defect type, pressure, and temperature are performed, similar to the approach in Ref. [48]. This generates a standard error of the mean for defect formation energy calculations of approximately 0.05 eV.

While at 0 K the dumbbell formation energy depends on the types of atoms it contains, at high temperatures, the formation energy computed using time-averaged system energies is averaged. For instance, a dumbbell may have diffused via a rotation-translation mechanism and changed the types (e.g., from U-U to U-Mo, etc.) multiple times during the calculation. Such an averaging process makes distinguishing between U and Mo unnecessary for obtaining the average formation energy and diffusivity. Such a distinction becomes necessary when self-diffusivities of U and Mo are of interest [39, 49]. Additionally, the formation energy of vacancies in random solid solution alloys, because they do not have chemical types, does not depend on the element type, as has been elucidated in the literature [48]. All defects are created this way to obtain the average defect properties without the need to distinguish U and Mo.

It should also be noted that, due to thermal effects, defects are able to reorient and relax to the preferable configuration.

The formation energy of a point defect is defined as:

$$E_f = E_f^{def} - \frac{(n \pm 1)}{n} E_f^{bulk} \tag{1}$$

where n is the total number of atoms in the system with no defects and E_f^{bulk} or E_f^{def} is defined as:

$$E_f^{def/bulk} = E^* - N_U \times E_U - N_{Mo} \times E_{Mo} \tag{2}$$

where E^* is the total energy of the system either with or without a defect, N_U is the number of U atoms in

---

[5]removed: interstitials, an

4

the system, E_U is the energy per atom of bcc U, N_{Mo} is the number of Mo atoms in the system, and E_{Mo} is the energy per atom of bcc Mo. The reference phases for U and Mo are the bcc phase at the temperature of interest. This formalism critically takes into account the non-zero formation energy of the alloy compound. The energy is defined for a given temperature and pressure, according to the system of interest.

The formation energy as defined by Equations (1) and (2) are in actuality a formation enthalpy [50]:

$$H_f = E_f + PV_f \tag{3}$$

where P is the applied pressure, V_f is the formation volume of a defect, and E_f is the formation energy at zero applied pressure. Typically, the PV term in Equation (3) is neglected as pressures are sufficiently small, and the formation enthalpy is treated as the formation energy, hence the utilized nomenclature when defining Equations (1) and (2). As will be shown, the formation enthalpy is sensitive to the applied pressure, and thus a formation volume can be identified. The formation volume itself is a function of composition and pressure and can be determined by looking at the slope of the formation enthalpy [..[6]](E+PV) with respect to pressure.

The elastic dipole tensor can be computed from the residual stress introduced by the insertion of a defect [51]:

$$\langle \sigma_{ij} \rangle = C_{ijkl}\epsilon_{kl} - \frac{P_{ij}}{V} \tag{4}$$

where $\langle \sigma_{ij} \rangle$ is the homogeneous stress of a periodic cell of volume V, ϵ_{kl} is the homogeneous strain applied on the supercell, C_{ijkl} are the elastic constants, and P_{ij} is the elastic dipole tensor. In this work, simulations are conducted in an NVT ensemble to determine formation energies and Equation (4) reduces to

$$\langle \sigma_{ij} \rangle = - \frac{P_{ij}}{V}. \tag{5}$$

This residual stress corresponds to the stress increase, after atomic relaxation, due to the insertion of a point defect in the supercell. Consequently, if the undefected system experiences a non-zero homogeneous stress, as is the case for applied stresses in this work, this contribution must be subtracted from the residual stress of the defective supercell to identify the elastic dipole tensor. The elastic dipole tensor is obtained for both vacancies and interstitials as a function of temperature [..[7]]and composition.

2.2. Diffusivity

To obtain the diffusivity of point defects in U-Mo systems, the same $14 \times 14 \times 14$ supercell of 5,488 atoms is utilized at a prescribed composition, and the same equilibration process is implemented, resulting

---

[6]removed: as a function of

[7]removed: , composition, and applied stress

in diffusion occurring in an *NVT* ensemble. Temperatures from 800 to 1400 K are explored, in increments
of 100 K. Compositions included bcc U, U-5Mo, U-10Mo, U-15Mo, U-30Mo, U-50Mo, and bcc Mo. Different
temperature ranges are explored for different compositions depending both upon the melting behavior and
the temperature above which diffusivity occurs. After defect insertion, the system is relaxed for 50 ps, after
which the mean-squared displacement (MSD) is tracked as a function of time. Diffusion of interstitials is
calculated over 10 ns. Because vacancy diffusion is slower than interstitial diffusion, simulations exploring
vacancies are conducted over 40 ns. The MSD is computed every 200 ps, and the slope of the MSD as a
function of time is utilized to determine the diffusion coefficient per Einstein's equation:

$$D = \frac{MSD}{6t}. \tag{6}$$

The diffusivity is determined over the entire simulation, and ten unique simulations are conducted to minimize
the impact of variations in compositional distributions. The MSD is verified to be linear as a function of
time, with typical R^2 values of a linear fit of > 0.95.

To observe the diffusion of point defects under a pressure gradient, an $80 \times 20 \times 20$ supercell consisting
of 64,000 atoms is constructed with periodic boundary conditions. The supercell is first relaxed in an *NPT*
ensemble for 100 ps to get the equilibrium dimensions of the system. Afterward, the system is further
relaxed 50 ps in an *NVT* ensemble. The temperature was held constant at 1200 K throughout the simulation.
To induce a pressure gradient in the x-direction of the supercell, 2 unit cell layers of atoms at both ends
($x \in [0, 2] \cup [78, 80]$) are made stationary, and the remaining 76 unit cell layers of atoms are given an additional
force in the x-direction. The added force is 0.005 eV/Å ramped over 1 ns. This produces a pressure gradient
of about [..[8]]0.3 kbar/Å, with a maximum compressive/tensile pressure of approximately $\pm$ [..[9]]50 kbar. A
point defect, either interstitial or vacancy, is then created in the middle of the supercell to detect its behavior
under a pressure gradient. The simulations are run for an additional 1 ns after the introduction of the point
defect. Atom positions are tracked throughout the simulations to detect lattice point jumps. Visualization
of these lattice jumps provides a way to track the point defect movement. One thousand unique simulations
with different initial conditions are run for each type of point defect. The final positions of the point defects
at the end of the simulations are recorded for the evaluation of point defect diffusion.

To evaluate the density of defects analytically, the 1D diffusion equation was solved using the implicit Euler
method. The zero flux boundary conditions were applied along with a discrete approximation of a Dirac delta

---

[8]removed: 0.03 GPa

[9]removed: 5 GPA

function as the initial condition. The following equations describe the system:

$$\frac{\partial c}{\partial t} = \frac{\partial}{\partial x}\left(D(x)\frac{\partial c}{\partial x}\right) \tag{7}$$

$$\frac{\partial c}{\partial x}\bigg|_{x=0} = \frac{\partial c}{\partial x}\bigg|_{x=275} = 0 \tag{8}$$

$$c(x,0) = \delta\left(x - \frac{275}{2}\right) \tag{9}$$

where $c \equiv c(x,t)$ denotes the density of a point defect at position x and time t, and $D(x)$ represents the diffusion coefficient of the point defect.

2.3. Radiation Damage

Radiation damage simulations are conducted from 600 to 1200 K in increments of 200 K. Pressures from -10 to 10 kbar are imposed hydrostatically on the system to investigate the effect of pressure on primary radiation damage generation in U-10Mo. A ZBL [52] potential is splined to the ADP with $r_{min} = 1$ Å and $r_{max} = 2$ Å. A supercell of $60 \times 60 \times 60$ unit cells is generated in the bcc structure with 21.6% of the atoms randomly set as Mo. The system is initially relaxed in an NPT ensemble for 50 ps at the target temperature. Supercell side lengths are averaged over the final 20 ps, and the supercell is scaled to the average lengths, with atomic positions remapped. The system is further relaxed in an NVT ensemble for 10 ps. A U atom in the center of the supercell is selected as the primary knock-on atom (PKA) and given a prescribed amount of kinetic energy. PKAs of 2, 4, 8, and 16 keV are explored in this work. The direction of the PKA is randomly selected, and twenty unique PKA directions are sampled. An adjustable timestep is utilized, with the maximum distance an atom can travel in a single timestep set to 0.05 Å, and a maximum timestep of 2 fs. The cascade simulation last for 50,000 timesteps, resulting in a total simulation time just shy of 100 ps. For systems at 1200 K, it was observed that the potential energy as a function of time (and the number of defects as a function of time) does not stabilize for the 16 keV PKA until approximately 120 ps. Thus, all systems at 1200 K were simulated for 75,000 timesteps, resulting in a total simulation time just shy of 150 ps. During the cascade, atomic motion is governed via an NVE ensemble with temperature rescaling to remove excess kinetic energy. This is similar to a recently published work by Yu et al. which demonstrated that this approach is appropriate [53]. The temperature rescaling in this work is more conservative than that of Yu, with a rescaling fraction of 0.05, and rescaling occurring every 100 timesteps. Validation simulations were performed for select cases and demonstrated statistically significant differences, emphasizing the robustness of this method. Defects are determined through the Voronoi tesselation method implemented within LAMMPS. The number of defects is determined as the average number of individual defects time-averaged over the final 5000 timesteps (10 ps) of the simulation to minimize effects from thermal fluctuations and residual shockwave impacts.

For context, the melting point of U-10Mo is determined from the two-phase melting method [54, 55] with a system size of $20 \times 20 \times 40$ unit cells consisting of 32000 atoms simulated for up to 1 ns. The melting point

188 was determined to be 1620 ± 10 K, which only slightly overestimates the experimental melting point of

189 approximately 1525 K [56]. Starikov [20] previously determined the melting point of pure U and Mo, finding

190 that the ADP slightly underestimates the melting point of U, and slightly overestimates the melting point of

191 Mo. Thus, the potential reasonably predicts melting points across the entire compositional range of γU-Mo

192 alloys.

3. Results

3.1. Point Defect Formation Energies

195 The temperature dependence of the nominal pressure defect formation energies is shown in Figures 1A and

196 1B. This figure is updated from [23] with additional simulations to improve the statistical certainty and briefly

197 discussed to provide the necessary context for the remainder of the results. For interstitials, the temperature

198 dependence undergoes an inflection point as a function of composition, in that in the U-rich regime, higher

199 temperatures lead to higher interstitial energies, while in the Mo-rich regime, higher temperatures lead to

200 lower interstitial energies. For vacancies, the trend of defect energy with temperature is consistent across

201 the compositional spectrum, in that higher temperatures lead to higher defect energies. The sensitivity of

202 this temperature dependence varies with composition, with the most temperature-sensitive compositions in

203 the U-rich regime. These results confirm an interstitialcy mechanism of self-diffusion via the lower defect

204 formation energy of interstitials, as outlined by prior authors [19, 20].

205 This underlying cause of the variation in formation energies as a function of composition is not known. The

206 nature of the formation energy is complex, related to a combination of electronic structure, formation enthalpies,

207 and elastic interactions. A study on an *ab initio* level would be required to fully explore the electronic structure

208 around defects at different compositions to attempt to identify the underlying cause of the observed behaviors.

209 We recommend this as a future study utilizing *ab initio* molecular dynamics.

210 The formation energy of interstitials and vacancies as a function of Mo atomic fraction at five unique

211 pressures and a temperature of 1200 K is shown in Figures 1C and 1D. Vacancies and interstitials exhibit

212 opposite trends as a function of applied pressure, as would be expected. As a crystal structure is compressed

213 (positive pressure), atoms are closer together than in the equilibrium case. As such, it would be expected

214 that a vacancy is more easily formed in the compressive state, and this is indeed observed. In the tensile

215 state (negative pressure), atoms are farther apart than at equilibrium and there is additional space between

216 the atoms. In this case, it would be expected that it is comparatively easier for an interstitial to form, and

217 this is indeed observed. However, the pressure sensitivity is not uniform for defect type and composition,

218 in that interstitials are the most sensitive to pressure at intermediate compositions (40-60 atomic percent),

219 while vacancies are the most sensitive to pressure in the U-rich regime.

220 The application of pressure does not affect the temperature dependence of defect formation energies,

221 nor does the temperature affect the trends of applied pressure on defect formation energies. However, it

222 does appear that at lower temperatures, the effects of pressure on interstitial formation energy are slightly
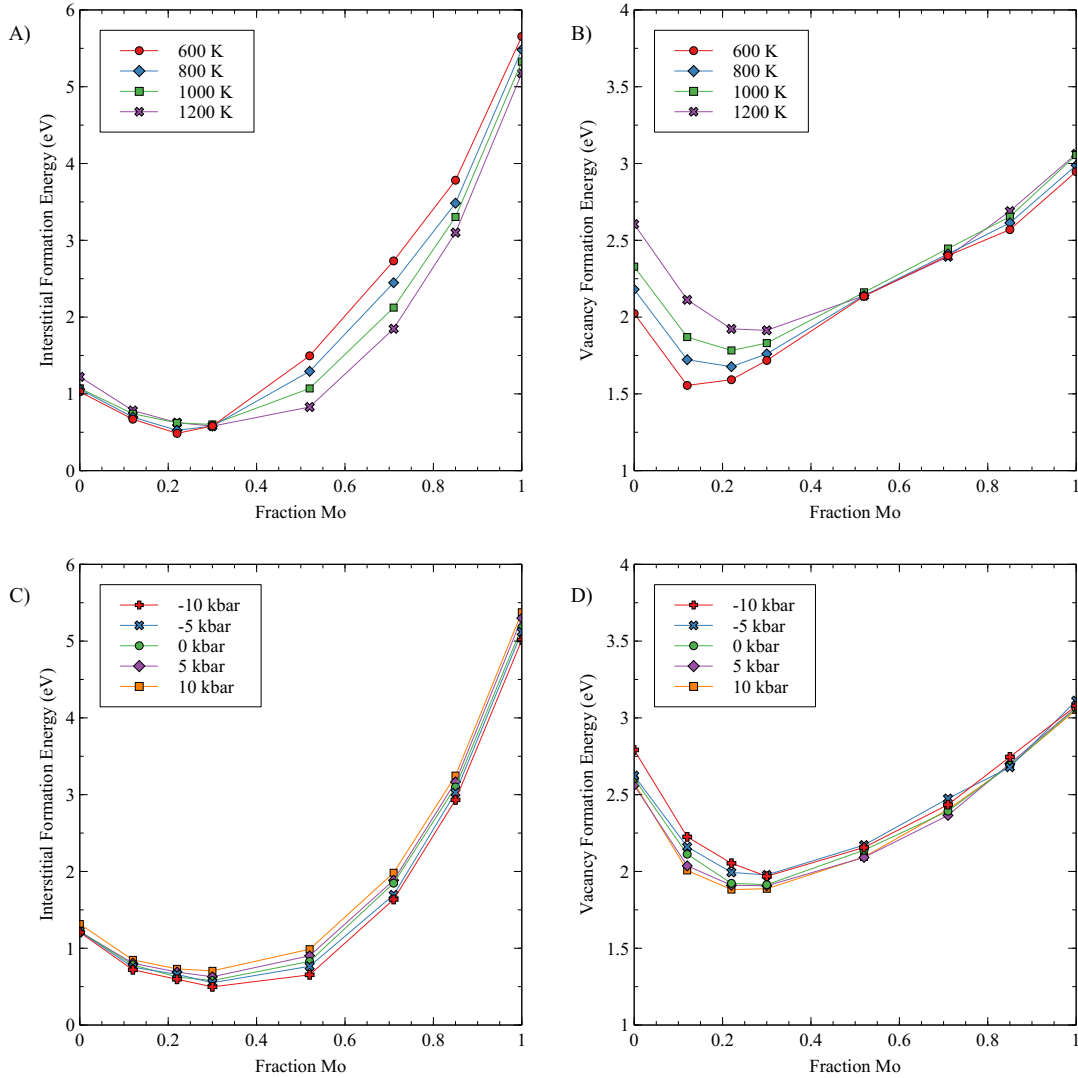
Figure 1: The variation of point defect formation energies in U-Mo as a function of composition, temperature, and pressure. A) The interstitial formation energy as a function of composition at four temperatures. B) The vacancy formation energy as a function of composition at four temperatures. C) The interstitial formation energy as a function of composition at five pressures. D) The vacancy formation energy as a function of composition at five pressures.

dampened. If the pressure sensitivity is gauged as a matter of relative change of defect formation energies, it is found that generally, vacancies are much less sensitive to pressure than interstitials and that sensitivity is not significantly affected by the temperature. However, since the magnitude of the vacancy formation energy is larger than the magnitude of the interstitial formation energy, the absolute (not relative) change in the defect formation energy with applied pressure is approximately the same for both interstitials and vacancies.

A note should be included on the choice of stress state. Only a hydrostatic stress state is applied in these systems. The actual stress state of the material may be more complex, consisting of bi-axial or uniaxial loading (shear loading is deemed unlikely). We have conducted preliminary studies on biaxial

9

²³² tension/compression and observed similar, but slightly lesser, trends in defect energetics. Prior studies have
²³³ shown a dependence of defect behaviors on deformation volume change [34, 57]. Thus, it is expected that
²³⁴ applied stress conditions that result in large volumetric changes (such as hydrostatic stress) will yield the
²³⁵ largest defect response. Therefore, other stress states were not pursued further and the data presented in
²³⁶ this manuscript can be considered an upper bound of the defect response to an applied stress.

²³⁷ The defect formation energies at all compositions, temperatures, and pressures are shown in Table A1
²³⁸ and Table A2.

3.2. Formation Volumes and Dipole Tensors

²⁴⁰ From Equation (3), the formation volume of a point defect at a specified composition and temperature
²⁴¹ can be determined from the slope of the formation enthalpy with respect to pressure. The formation volume
²⁴² of interstitials and vacancies as a function of composition at different temperatures is shown in Figure 2.
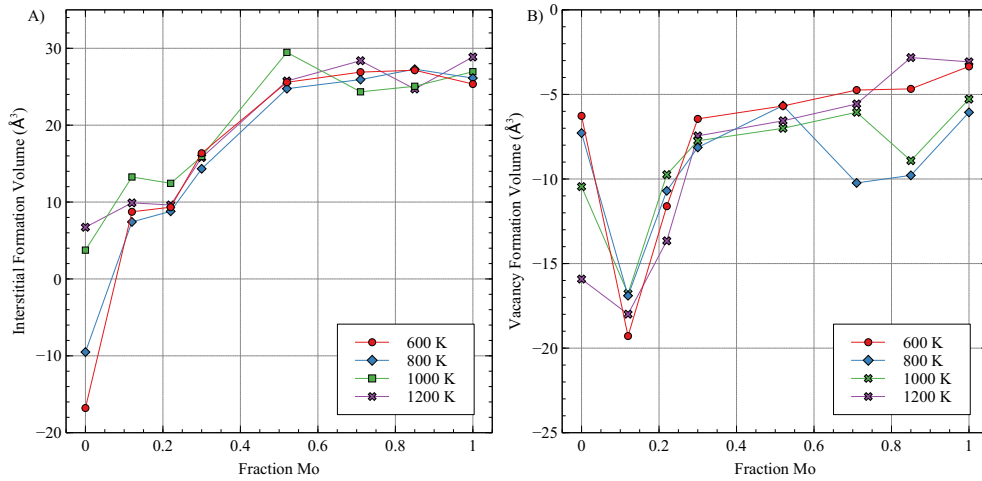

Figure 2: The defect formation volume of A) interstitials and B) vacancies in U-Mo alloys as a function of Mo content at four different temperatures.

²⁴³ There are a number of interesting trends that emerge when analyzing the defect formation volumes. Let us
²⁴⁴ begin by looking at the 1200 K data, where the interstitial shows a positive formation volume over the entire
²⁴⁵ compositional range, and slightly increases with Mo content up to 50% Mo, after which the defect formation
²⁴⁶ volume is approximately constant. For vacancies, we observe negative formation volumes across the entire
²⁴⁷ composition and again show a general increase with Mo content. The plateauing behavior for vacancies in
²⁴⁸ U-Mo occurs for concentrations of greater than 30% Mo. These are generally expected behaviors, but the
²⁴⁹ compositional trends are novel to this system. For all alloy systems (non-zero concentration of Mo), these
²⁵⁰ trends are generally consistent, showing some deviation, but retaining the same behaviors. There is some
²⁵¹ minor unexplained variance at high Mo content for the vacancy formation volume, however, the error bars
²⁵² (not shown for clarity) still overlap. For completeness, each data point shown in Figure 2 is the product of
²⁵³ a fit, and the standard error of that regression analysis was determined. These standard errors generally
²⁵⁴ increase with temperature and decrease with higher Mo content.

In exploring lower temperatures without Mo, we begin to deviate from the expected behavior. At 600 and 800 K, the interstitial has a negative defect formation volume. This indicates that with a higher compressive stress, the formation enthalpy of the interstitial decreases. As stated, this is counter-intuitive to our typical notion of the relationship between interstitials and pressure, in that they should have a lower formation enthalpy in systems under tension, where there is additional space in the lattice to accommodate them. There are two important points to note in order to properly contextualize this result. First is the difference between the relaxation volume and the formation volume. The relaxation volume is the change in the volume of a supercell upon the insertion of a defect. This relaxation volume is analogous to a change in pressure in a fixed-volume system, which is the case in this work, and will be discussed in the dipole tensor section. Thus, a negative formation volume does not equate to a negative relaxation volume. Second, the γ phase of pure U is mechanically unstable at low temperatures [58] and becomes stabilized with the addition of Mo. The interatomic potential utilized in this work can predict a metastable γ phase at all temperatures investigated, however, based on the behavior of the formation volumes, it is clear that the U-rich structure is nearing the point of instability. Therefore, as we approach the stability limit of the γ phase, an increase in the compressive stress leads to lower formation energies of interstitials. These stability effects are also observed for vacancies, in that as the temperature of pure γ U decreases, the formation volume of vacancies increases (becomes less negative). This behavior is the converse of that observed for interstitials. It is our recommendation that defect formation volumes that indicate instability (those for γ U below 1000 K), should not be utilized for higher-length scale studies. However, they are included here to demonstrate the behavior of this system, and how mechanical instabilities impact the thermodynamic behavior of defects, even if the structure itself remains stable.

In the computation of the elastic dipole tensor using Equation (5), it was found that there are no significant off-diagonal components, and the induced stresses are isotropic (within the statistical certainty), which simplifies the calculation. Thus, the homogeneous stress is simply the trace of the stress tensor divided by 3. The elastic dipole tensor for U-Mo for interstitials and vacancies as a function of Mo content at four different temperatures is shown in Figure 3.

It should be noted that the induced isotropic stresses are due to the nature of interstitials at elevated temperatures, which are able to rotate and change orientation. The migration energy of interstitials in U-10Mo has been observed to be approximately 0.33 eV [49], and the barriers for rotation are expected to be significantly lower. Taking a time-average of the elastic dipole tensor necessarily means that we are sampling different configurations of interstitials and seeing an average behavior that results in an isotropic elastic response. This is distinctly different from exploring specific dumbbell configurations in bcc lattices at 0 K.

The elastic dipole shows the relative amount of residual stress exerted by each species on the U-Mo system. Interstitials show clear trends with respect to both composition and temperature. The elastic dipole increases monotonically with increasing Mo content. However, there is an inflection point at 30% Mo where the temperature trends reverse. Below this composition, an increase in temperature increases the
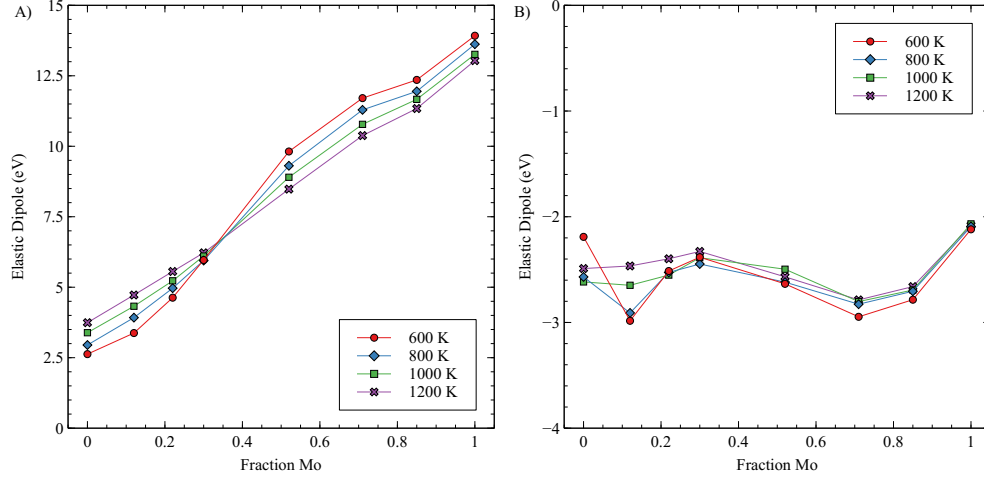
11

Figure 3: The elastic dipole tensor in U-Mo for A) interstitials and B) vacancies as a function of Mo content at four different temperatures.

elastic dipole, and above this composition, it decreases the elastic dipole. This inflection mirrors that of the formation energy shown in Figure 1A. Thus, the formation energy is directly linked with the induced stress in the lattice from the inserted interstitial. The behavior of vacancies is more convoluted, as there are minimal changes across the entire compositional and temperature spectrum in the dipole tensor. The relative magnitude of the dipole tensor for vacancies is less than that of interstitials and possesses the opposite sign, indicating induced tensile stress instead of the observed compressive stress from interstitials.

[..[10]]

3.3. Point Defect Diffusivities

In this subsection, the diffusivities of interstitials and vacancies are studied as a function of composition, temperature, and pressure. This is the most thorough examination of point defect diffusive properties within the literature for zero pressure, and the only study to date exploring the effect of non-zero pressures. Data utilized to generate the plots in the following subsection are included in the appendix for completeness.

3.3.1. Diffusion as a Function of Concentration

The diffusion coefficient of interstitials and vacancies as a function of temperature for different U-Mo compositions is shown in Figure 4. The plots for interstitials (A) and for vacancies (B) are shown on the same scale to make comparisons easier. Seven compositions are explored: bcc U, U-5Mo, U-10Mo, U-15Mo, U-30Mo, U-50Mo, and bcc Mo, where concentrations are given in weight percent. The temperature ranges

---

[10]removed: The impact of applied stress on the dipole tensor is also analyzed. For interstitials, there is a very slight positive correlation with pressure, in that a larger compressive stress leads to a higher elastic dipole. Vacancies have a similar magnitude trend, but in the opposite direction, exhibiting a lower elastic dipole under compressive stress. However, these effects are quite small, in that the total change in the elastic dipole for a given temperature and composition, considering the entire range of stresses (-10 to 10 kbar), is approximately 0.3 eV. This figure applies to both interstitials and vacancies, but, as stated, the direction of the impact is opposite for the two defect types. Thus, the magnitude of the stress has a minor impact on the defect elastic dipole.

over which diffusivities have been collected vary, as statistically significant diffusive behaviors are observed over different temperature regimes, due to the varying migration energies as a function of composition.

The point defect diffusivity is always highest in bcc U, and tends to decrease with increasing Mo content. This decrease is monotonic for vacancies, in that bcc Mo displays the slowest diffusivity. However, for interstitials, the slowest diffusion is observed for U-50Mo. Typically, the slopes of these curves are less steep for interstitials than for vacancies, indicating smaller migration barriers, as expected. The migration barriers can be extracted from Arrhenius fits to each composition-defect data set.
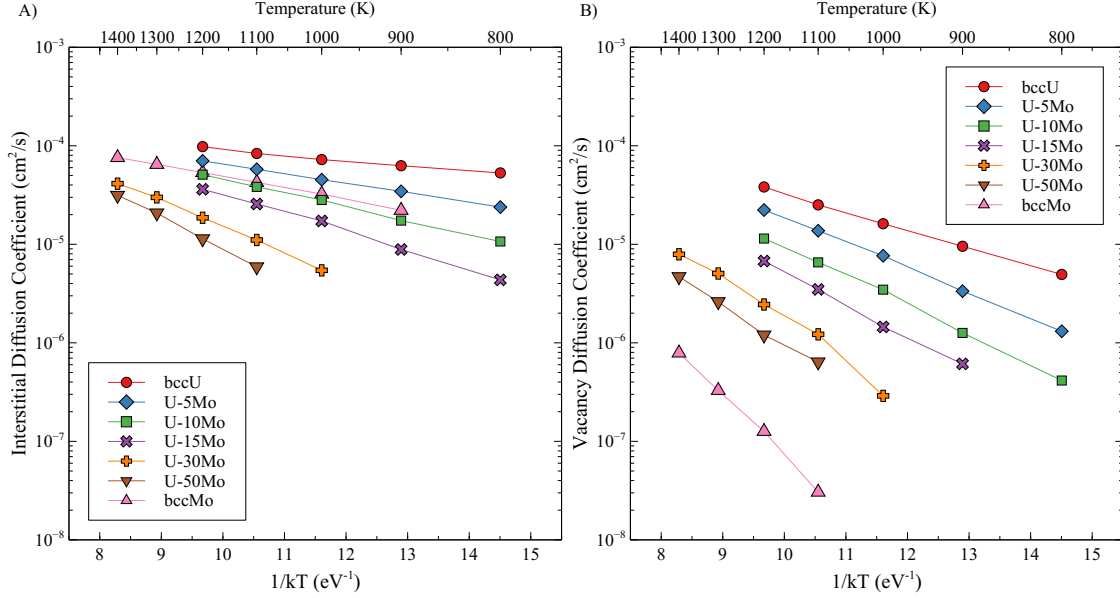

Figure 4: The diffusion coefficient of A) interstitials and B) vacancies as a function of Mo concentration and temperature.

To more clearly illustrate the differences with respect to composition, the diffusion coefficient of interstitials and vacancies at 1200 K is plotted as a function of Mo concentration in Figure 5. There is a nearly linear function of the vacancy diffusion coefficient as a function of Mo, decreasing with additional Mo present within the alloy. However, for interstitials, there is a minimum at U-50Mo, and the diffusion coefficient increases for bcc Mo, to a level comparable to U-10Mo. To better elucidate the underlying effects, the migration barrier and the pre-factor for interstitials and vacancies as a function of Mo concentration are shown in Figure 6.

The migration barrier displays a very similar trend to the overall diffusivity, as would be expected, as this term lies within an exponential, and thus would likely have a stronger impact on the diffusivity than the prefactor. While monotonically decreasing for vacancies, the trend becomes less linear and is more appropriately fit by an exponential decay for concentrations from bcc U up to U-50Mo. This is followed by a steeper drop to the value of the migration energy for bcc Mo. It should be noted that migration barriers here are denoted as negatives, but this should be taken simply as the numerator in the Arrhenius function. This choice was made to more clearly illustrate comparisons between Figures 5 and 6, in that a larger migration barrier (more negative value) decreases the diffusion coefficient. Thus, bcc Mo displays the highest migration barrier of all systems shown for vacancies. The interstitial migration barrier follows nearly an identical trend
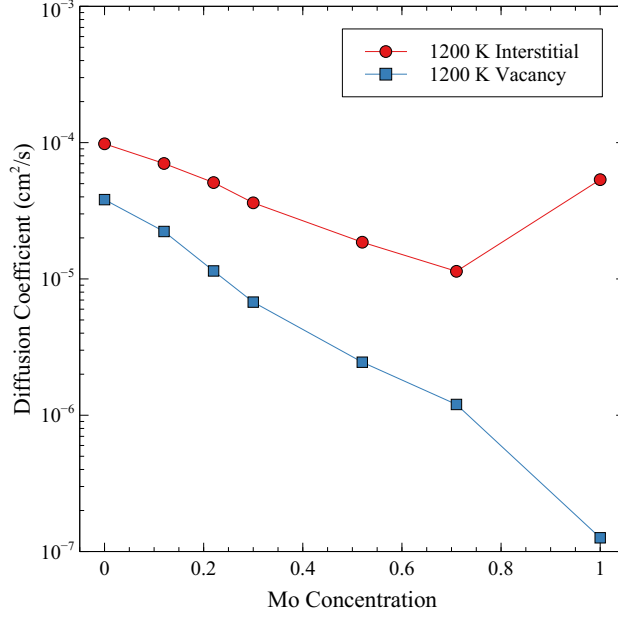
13

Figure 5: The diffusion coefficient of interstitials and vacancies as a function of Mo concentration at 1200 K.

to the interstitial diffusivity shown in Figure 5.

The prefactor shows more complex behavior but retains the discontinuity at a concentration of U-50Mo. The prefactor for interstitials displays an inverse behavior to that of the migration barrier, where it peaks at a concentration of U-50Mo and shows a minimum at bcc U. For vacancies, the prefactor is at a maximum for bcc Mo and a minimum for bcc U. In all of these systems, there is a clear delineation between the alloy behavior and the behavior of bcc Mo. Compositional dependence can readily be determined from bcc U up to U-50Mo, but there is a change in the diffusive behavior once Mo content exceeds 50 wt.%. The origin of this piecewise-type behavior is unknown but potentially relates to the low-temperature instability of the bcc U phase and its potential impacts on modifying the alloy structure of U-Mo systems. Since higher Mo concentrations in the alloy were not studied (i.e., greater than 50 wt.% but less than 100 wt.%), the actual composition at which this inflection is present is unknown. Since U-rich Mo alloys are of primary interest, the Mo-rich portion of the alloy composition was sampled with less frequency in this work and is recommended as an area of potential future study.
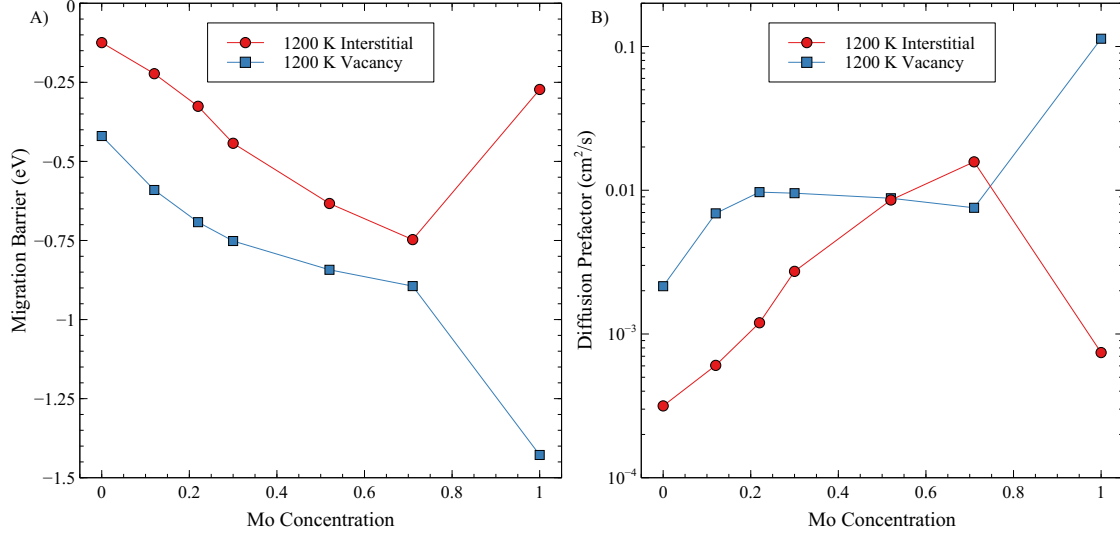
Figure 6: The A) migration barrier and B) diffusion prefactor of interstitials and vacancies in U-Mo as a function of Mo concentration. The migration barrier shown is the numerator in the Arrhenius equation for ease of comparison.

3.3.2. Diffusion as a Function of Pressure

The diffusion coefficient for interstitials and vacancies for U-10Mo as a function of applied pressure at five different temperatures is shown in Figure 7. As in the study on formation energies, hydrostatic pressure is applied, ranging from -10 to +10 kbar [..[11]]in magnitude. The first observation is that the effects are quite minimal. For all data presented, the total magnitude of the diffusion coefficient changes by less than a factor of 2. Comparing this to the compositional effects presented earlier in this subsection where diffusion coefficients varied by up to 3 orders of magnitude, this indicates a nearly pressure-independent behavior. However, trends are present, albeit in a small magnitude. One would expect that for interstitials, a decrease in pressure, which yields an expansion of the lattice, would allow for faster interstitial diffusion. This is generally the case, where more negative pressures yield slightly higher diffusivities. For vacancies, we would expect the opposite trend, in that a compressive stress pushes atoms closer together, decreasing the jump path length, and subsequently increasing the vacancy diffusivity. This trend is not evident, as there is effectively no statistically significant difference in the vacancy diffusivity as a function of pressure. It should be noted that error bars are not shown on these plots for the sake of clarity, but all data shown has a standard deviation of less than 10% for interstitials and less than 15% for vacancies, with the standard deviation decreasing with increasing temperature.

This data was analyzed as a function of temperature for all compositions and displayed a marginally greater influence of pressure at lower temperatures, but this finding was not statistically significant. Thus, the behaviors were averaged across temperatures to identify the general compositional trends with applied pressure. To do so, the slope of the diffusivity versus pressure data (displayed in Figure 7) was averaged over all temperatures explored at each composition. This slope versus pressure data tells us whether the

---
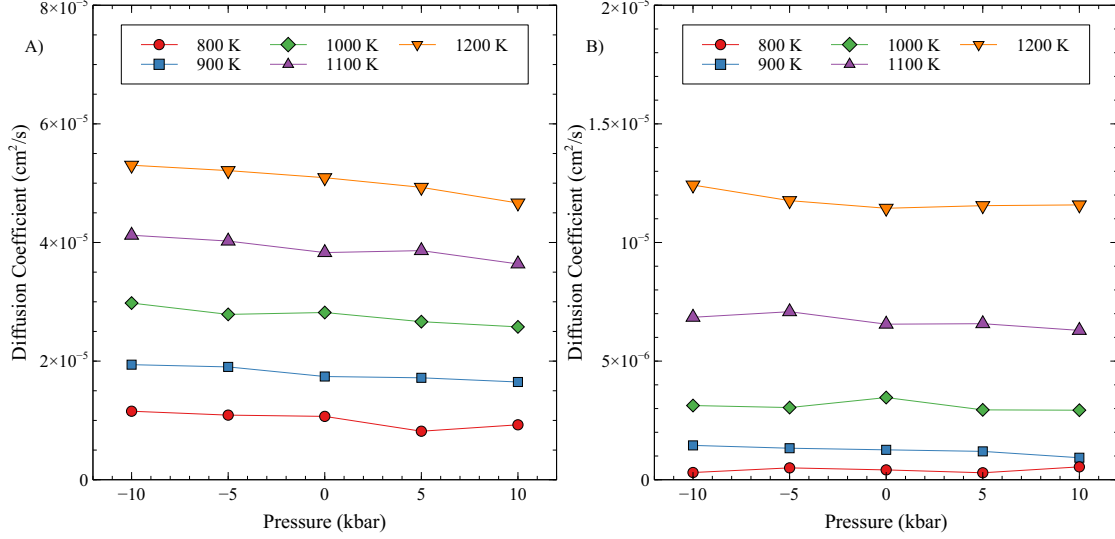
[11]removed: (-1 GPa to +1 GPa)

15

Figure 7: The diffusion coefficient of A) interstitials and B) vacancies in U-10Mo as a function of pressure.

diffusivity is positively (compressive stress increases diffusivity) or negatively (tensile stress increases diffusivity) correlated. This data is displayed in Figure 8. For vacancies, the pressure has no statistically significant impact on diffusivity for Mo concentrations greater than U-5Mo. However, for bcc U, there is a pronounced impact in that compressive stresses increase vacancy diffusivity. For interstitials, there is a negative value of the slope of diffusivity versus pressure for all U-Mo compositions, indicating tensile stresses increase interstitial diffusivity. Interestingly, for bcc U, the interstitial diffusivity is slightly increased under compressive stresses. This may relate to a Crowdion mechanism [59] in bcc U which can potentially become more favorable under compressive stresses. However, this effect was not fully quantified. A slight positive correlation for interstitials in bcc Mo was also observed, but this result is not statistically significant, and thus it is concluded that applied pressure has a negligible impact on interstitial diffusivity in bcc Mo.

Thus, while there are clear trends identified for the effects of pressure on interstitial diffusivity, these impacts are quite small, and should only modify the magnitude of the defect diffusivity by less than a factor of two. Additionally, there is no statistically significant impact of pressure on vacancy diffusion for U-Mo alloys, but only for bcc U. To verify these findings in a more realistic scenario with variable stresses, diffusion under a pressure gradient was explored, as outlined in the following subsection.
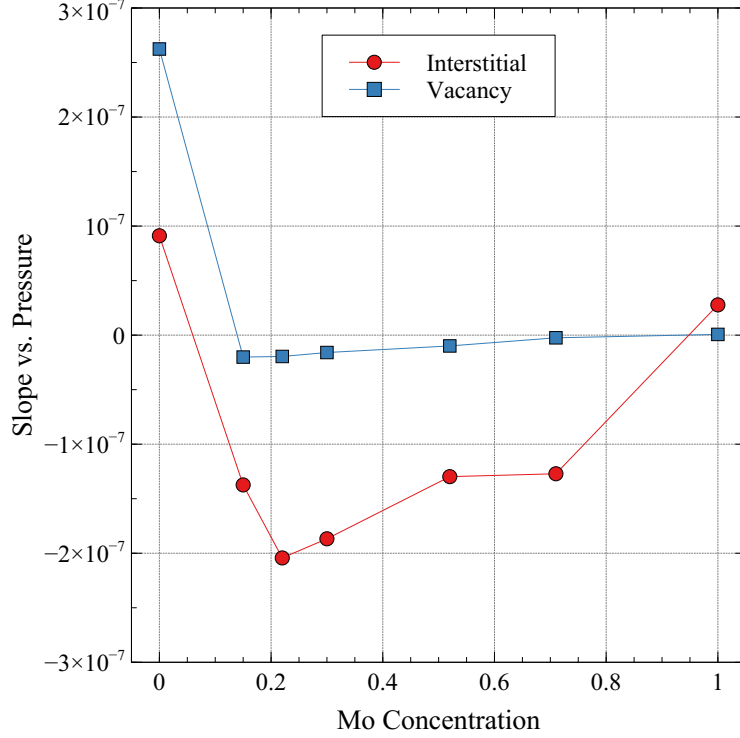
16

Figure 8: The temperature-averaged slope of the diffusion coefficient versus pressure as a function of Mo concentration.

3.4. Diffusion Under a Pressure Gradient

For the evaluation of point defect diffusion, a supercell with externally added force in one direction is simulated as described in the computational details. Figure 9[..[12]]a shows the resulting pressure gradient in the x-direction of the supercell. The simulation box is approximately 275 Å long in the direction of the pressure gradient. The point defects, either an interstitial or a vacancy, are introduced at x = 137.5 Å. The trajectories of the point defects are determined by tracking single lattice point jumps. Figure 9[..[13]]b depicts the point defect movement as colored vectors. A red vector denotes a jump by a U atom, while a blue vector denotes that of a Mo atom. The figure omits the z coordinate for brevity. From the figure, it can be observed that the point defect movement is mainly facilitated by the U atoms[..[14]], with some, but less, diffusion via Mo atoms. There are two reasons for that: 1) U atoms make up 78 at.% of the alloy, and 2) U atoms have a higher self-diffusivity than that of Mo atoms. Overall, the point defect motion resembles a random walk. To collect the statistics of point defect motion, data is aggregated from one thousand simulations for each type of point defect. Figure 9[..[15]]c displays violin plots with embedded boxplots of point defect final positions at the end of the simulations. The dashed vertical line in the middle represents the starting position of the point defects. The interquartile ranges of both types of point defects contain the initial position. The final

---

[12]removed: A
[13]removed: B
[14]removed: with little help from the
[15]removed: C

394 positions of the vacancies are more centralized than that of interstitials. This is expected since interstitials
395 generally move faster than vacancies. The mean final position of interstitials is $x = 125$ Å, while the standard
396 deviation is 40 Å. For vacancies, the mean is $x = 123$ Å, and the standard deviation is 27 Å. [..[16]]Thus,
397 there is not a statistically observable effect of the pressure gradient on diffusion in these MD simulations.

[..[17]]
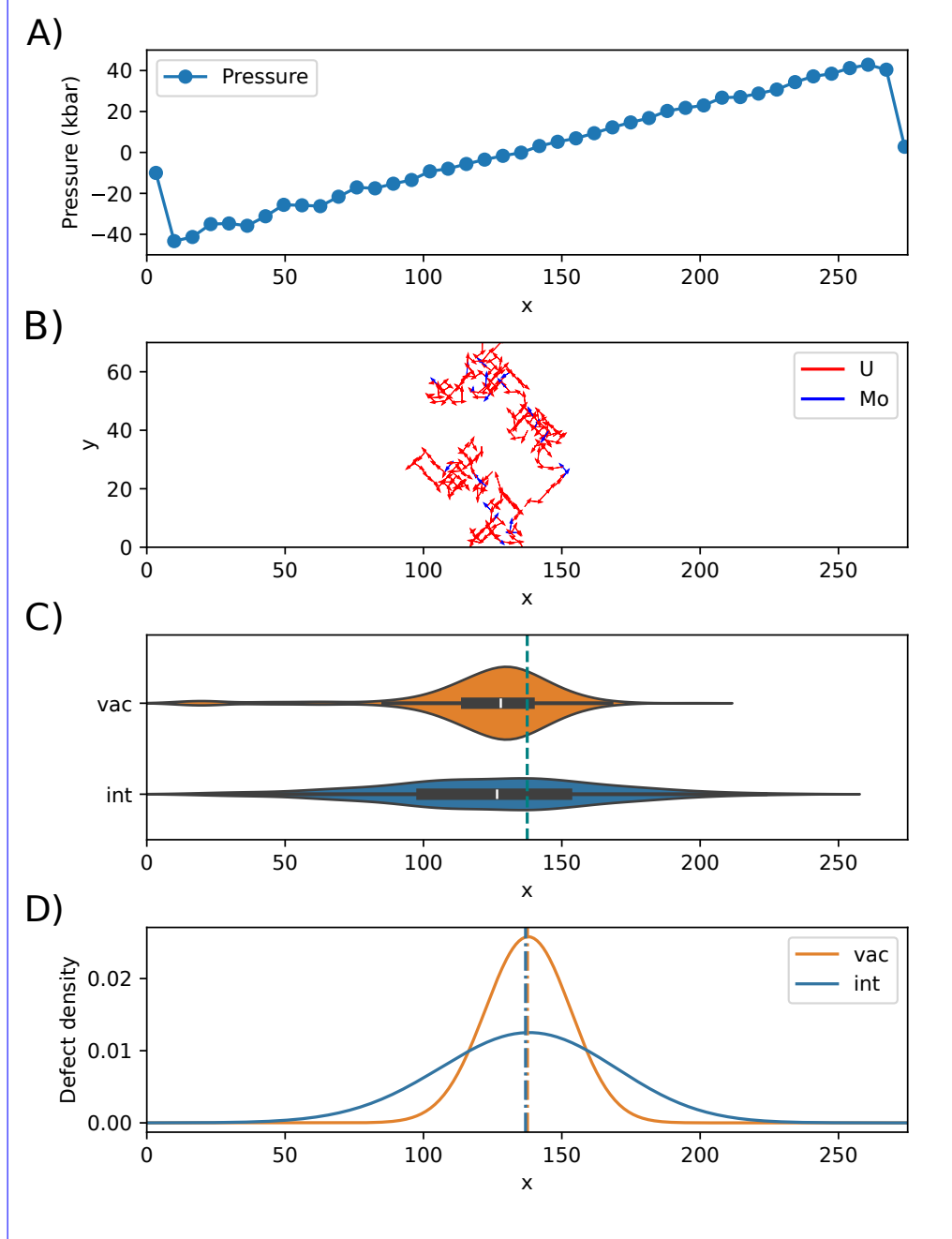
Figure 9: A) Pressure Gradient along the x-axis in the supercell. B) Trajectory of an interstitial defect. C) Violin plots of point defect final positions at the end of simulations. D) Analytical point defect density after 1 ns.

---

[16]removed: Even though the mean final positions are toward the region with lower pressure for both types of point defects, we cannot conclude any directional preference due to the large standard deviations. As such, there is not enough evidence to claim that the pressure gradient in the alloy affects point defect diffusion.

The 1-D diffusion equation was solved using Equation (7) to analytically evaluate the effect of pressure gradient on defect diffusion. Figure 7 provides diffusion coefficients of point defects as a function of pressure and temperature. Linear fits to that data were utilized to obtain analytical forms of the diffusion coefficients at 1200 K. Since the pressure gradient is a linear function of position x, the diffusion coefficient becomes position-dependent as well. The equations below provide the fitted linear functions:

$$D_{int}(x) = -2.5 \times 10^{-7} P(x) + 5.1 \times 10^{-5} \tag{10}$$

$$D_{vac}(x) = -5.5 \times 10^{-8} P(x) + 1.2 \times 10^{-5} \tag{11}$$

$$P(x) = -44.4 + 0.35(x - 9) \tag{12}$$

398 where $D(x)$ is in cm^2/s, $P(x)$ is in kbar, and x is in Å.

399 Figure 9d shows the point defect densities after 1 ns as derived from the diffusion equation. The dash-dotted

400 vertical lines denote the expected value of x. The defect density distributions are marginally skewed to the left.

401 These analytical density distributions show similarities to the kernel density estimations portrayed in Figure 9c,

402 thereby validating the results from the MD simulations. The two noticeable dissimilarities are the presence of

403 outliers in the tensile pressure region of the supercell and the difference in the average/expected positions of the

404 point defects between the simulation and analytical results. While the average final position of the defects in

405 the simulations is about 10 Å away from the starting position, the analytical solution to the diffusion equation

406 suggests that the average final position should be closer to the center. The discrepancy might have arisen due

407 to the non-linear nature of the pressure gradient at the edges of the simulation supercell. Additionally, the local

408 pressure values in the simulations oscillate with time and are affected by the introduction of point defects in

409 the vicinity. Due to these unavoidable factors, slight quantitative discrepancies between simulation results and

410 analytical solutions are expected. Regardless, the results from the MD simulations and the analytical exploration

411 are in remarkable agreement, and do not show a significant segregation of defects under a pressure gradient, but

412 only a slight skewing of the density of point defects toward the tensile pressure region.

413 *3.5. Radiation Damage*

414 The number of defects generated in U-10Mo as a function of pressure for PKAs of 2, 4, 8, and 16 keV at

415 600, 800, 1000, and 1200 K is shown in Figure 10. At lower temperatures, regardless of PKA energy, there

416 is minimal effect of the pressure on the total number of defects generated. Every set of data displayed below

417 1200 K shows an effectively zero slope with respect to pressure. However, at 1200 K, there is a clear trend, in

418 that compressive stresses (positive) inhibit the generation of defects, while tensile stresses (negative) enhance

419 defect generation. The relative increase with applied pressure at 1200 K results in an increase in the number

420 of defects generated of approximately 24% for a -10 kbar tensile stress, and a corresponding decrease in

421 the number of defects generated of approximately 14% for a 10 kbar compressive stress. Error bars are not

422 shown for the sake of clarity, but the standard deviation of the sample set is approximately 20% of the mean

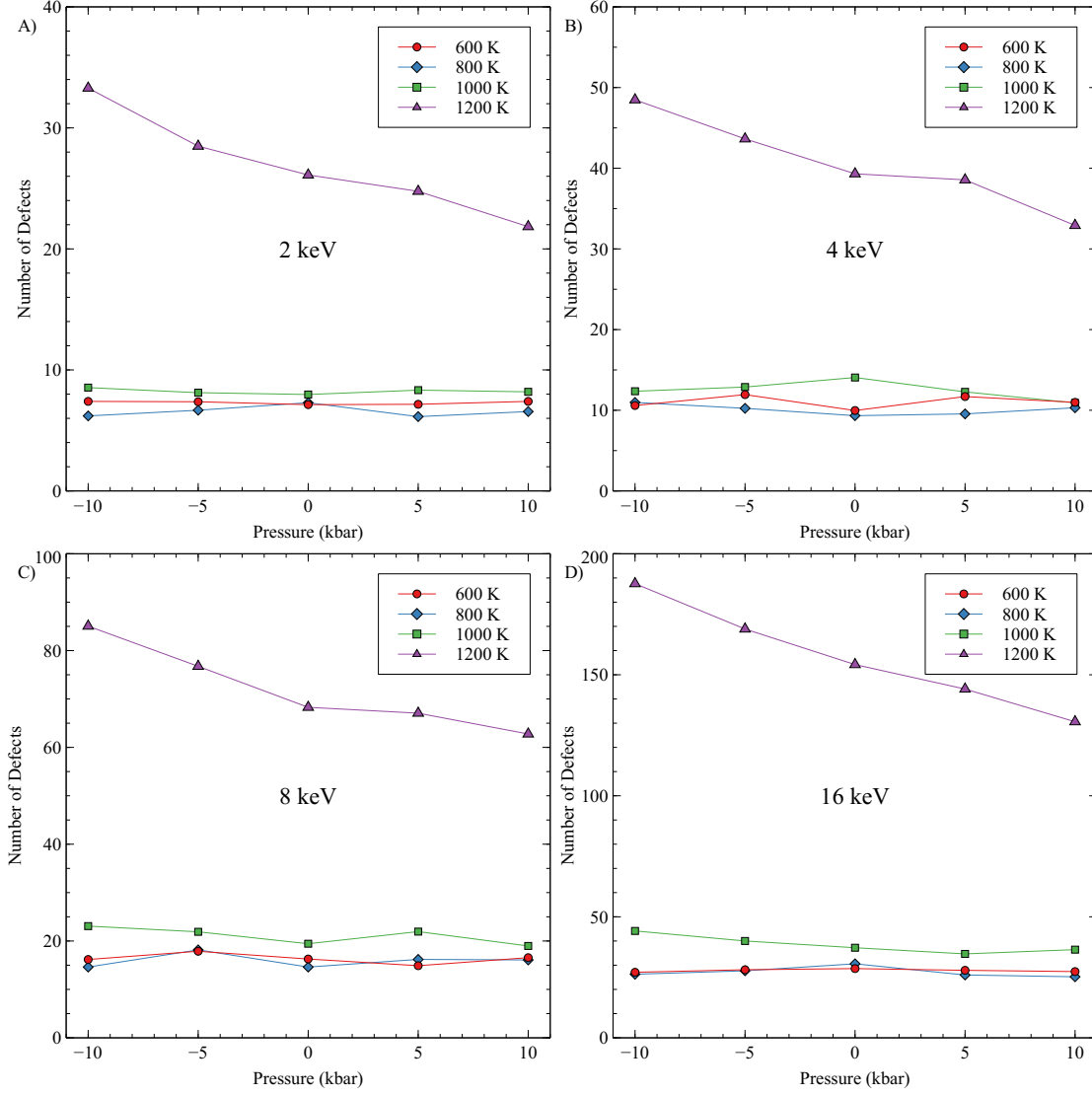423 value for each temperature, PKA energy, and pressure.

19

Figure 10: The number of Frenkel pairs generated in U-10Mo as a function of pressure at four temperatures and PKA energies of (A) 2 keV, (B) 4 keV, (C) 8 keV, and (D) 16 keV.

The second trend observed from the figures is the increase in the number of defects with increasing temperature. From 600 to 800 K, there is no statistically significant difference in the number of defects. However, from 800 to 1200 K, the number of defects increases exponentially with the temperature for all PKA energies. The exponential increase takes the form of $A \times e^{BT}$, where A ranges from 0.33 to 0.68, and B ranges from 0.0035 to 0.0044, with increasing values of A and B with increasing temperature. These trends are statistically significant, with $R^2 > 0.93$. Thus, as the system approaches the melting point ($T > 0.5T_m$), it becomes significantly easier to generate defects. This is despite the fact that for U-10Mo the defect formation energies slightly increase with increasing temperature. This is believed to be due to the fact that the cascade can more readily produce a localized melted zone during the thermal spike phase, producing more defects. While additional recombination is expected to take place at higher temperatures, this will lead to

20

For the primary application of interest in this work, research reactors, the operating temperature is below 600 K [60]. Thus, we do not expect to see significant effects of the pressure on defect generation, and we expect that the number of defects generated at temperatures below 600 K to be approximately equal to the data collected here at 600 K, due to the observed trends at higher temperatures.

The collected data for each temperature at a zero pressure state are collected and displayed in Figure 11. Power-law fits are obtained by examining the number of defects as a function of PKA energy at different temperatures. Power-law fits are chosen as they more readily fit MD data than the historical NRT [61] or Kinchin-Pease (K-P) [62] equations, as in Miao [26]. The NRT/K-P models do not take into account recombination, as has been outlined by Nordlund [63]. The power-law fits change dramatically with increasing temperature, but converge at lower temperatures, with the data for 600 and 800 K essentially overlapping. All lower temperatures are expected to follow the behavior in these "low temperature" curves. Such equations can be utilized to determine the number of residual defects from irradiation damage with more accuracy than the NRT model.
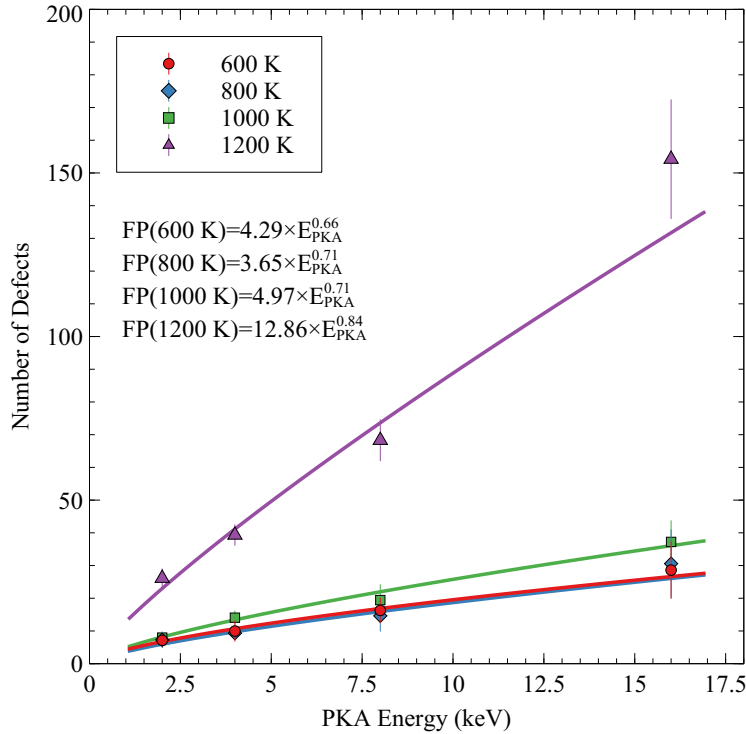

Figure 11: The number of Frenkel pairs generated in U-10Mo as a function of PKA energy. Fits for each temperature of the form $A \times E_{PKA}^{B}$ are included, where E_{PKA} is the PKA energy in keV.

It should be emphasized that radiation damage cascades were only conducted in U-10Mo, and thus there is no compositional dependence explored here. The fundamental nature of the residual radiation damage and the impact of composition are the subject of a future study.

4. Conclusion

This work investigated how the hydrostatic tension and compression affect the formation energy of interstitials and vacancies as a function of pressure, temperature and composition in U-Mo. On average, the maximum applied pressure of 10 kbar produces a 6% increase in the interstitial formation energy and a 3% decrease in the vacancy formation energy. Under reasonable applied bulk pressures below the yield point (<100 MPa), negligible deviations in the defect formations are observed. There are impacts of the applied pressure on defect formation and clear trends can be observed, but these effects are sufficiently small, even at large pressures, that they likely can be neglected for practical purposes. However, in circumstances where the pressures may be quite large, e.g., in the area surrounding a highly pressurized nanometer-sized bubble, statistically significant changes in the local defect formation energy could be observed[..[18]].

The effect of applied pressure of the diffusion of point defects was also explored. The diffusion of interstitials and vacancies are only slightly modified as a function of pressure, but do show a linear dependency, with slightly faster rates of diffusion under tensile stress. Subsequently, diffusion under a pressure gradient was investigated for U-10Mo, which showed a slight skewing of the defect density towards the tensile region, observed both from MD simulations and from an analytical solve using the pressure-dependent diffusion equations. Thus, applied pressure or pressure gradients appear to have minimal impacts on the diffusivity or segregation of defects.

Finally, the effect of pressure on radiation damage was investigated for different compositions, temperatures, and cascade energies. The effects of pressure become appreciable at elevated temperatures, with additional defects being generated under high tensile loading. At lower temperatures relevant for research reactors, there is effectively no impact of pressure on the cascade behavior or the resultant number of Frenkel pairs produced from a given cascade. The stable number of Frenkel pairs follows a power law, and can be expressed at 600 K as $FP = 4.3 \times E_{PKA}^{0.66}$.

This work has provided a comprehensive investigation into the behavior of point defects [..[19]]under applied stresses in U-Mo alloys. This work can be incorporated into mesoscale and engineering scale modeling tools that include defect-stress interactions to describe complex phenomena such as fuel creep and fission gas swelling.

5. Acknowledgements

---

[18]removed: , potentially altering fission gas bubble evolution and creep behaviors. This work provides the basis for expansion to investigate the effects of applied pressure on defect diffusion, the behavior of defects under a stress gradient, and the generation
[19]removed: due to applied pressure

22

DE-AC07-05ID14517. This manuscript has been authored by Battelle Energy Alliance, LLC with the U.S. Department of Energy. The publisher, by accepting the article for publication, acknowledges that the U.S. Government retains a nonexclusive, paid-up, irrevocable, worldwide license to publish or reproduce the published form of this manuscript, or allow others to do so, for U.S. Government purposes. This research made use of the resources of the High Performance Computing Center at Idaho National Laboratory, which is supported by the Office of Nuclear Energy of the U.S. Department of Energy and the Nuclear Science User Facilities.

6. Conflict of Interest

The authors declare no competing financial interest.

7. Data Availability

Data will be made available upon request to the corresponding author.

8. Appendix

8.1. Defect Formation Energies

Table A1: Formation Energy of Interstitials in U-Mo. Pressure in units of kbar and formation energies in units of eV.

Pressure	bcc U	U-5Mo	U-10Mo	U-15Mo	U-30Mo	U-50Mo	U-70Mo	bcc Mo
1200 K								
-10	1.21	0.72	0.60	0.50	0.65	1.64	2.93	5.01
-5	1.22	0.75	0.66	0.55	0.77	1.69	3.03	5.12
0	1.22	0.78	0.63	0.58	0.83	1.85	3.10	5.18
5	1.21	0.80	0.69	0.63	0.90	1.88	3.17	5.30
10	1.31	0.85	0.73	0.71	0.99	1.98	3.25	5.38
1000 K								
-10	1.05	0.68	0.53	0.50	0.84	1.97	3.13	5.15
-5	1.08	0.68	0.57	0.53	1.00	2.06	3.23	5.28
0	1.07	0.74	0.62	0.60	1.07	2.12	3.30	5.33
5	1.10	0.79	0.66	0.64	1.13	2.18	3.34	5.41
10	1.09	0.83	0.68	0.69	1.23	2.29	3.47	5.51
800 K								
-10	1.12	0.61	0.50	0.49	1.10	2.28	3.33	5.36
-5	1.09	0.64	0.52	0.50	1.19	2.33	3.41	5.45
0	1.06	0.70	0.53	0.58	1.29	2.45	3.48	5.48
5	1.04	0.68	0.56	0.61	1.37	2.49	3.59	5.59
10	1.00	0.70	0.61	0.66	1.39	2.60	3.67	5.70
600 K								
-10	1.14	0.58	0.43	0.48	1.33	2.55	3.60	5.51
-5	1.09	0.61	0.44	0.54	1.42	2.66	3.69	5.60
0	1.03	0.67	0.49	0.58	1.50	2.73	3.78	5.66
5	0.96	0.70	0.51	0.65	1.56	2.79	3.86	5.75
10	0.94	0.68	0.55	0.68	1.66	2.91	3.95	5.83

23

Table A2: Formation Energy of Vacancies in U-Mo. Pressure in units of kbar and formation energies in units of eV.

Pressure	bcc U	U-5Mo	U-10Mo	U-15Mo	U-30Mo	U-50Mo	U-70Mo	bcc Mo
1200 K								
-10	2.79	2.23	2.05	1.97	2.16	2.44	2.75	3.08
-5	2.62	2.16	1.99	1.98	2.17	2.47	2.68	3.11
0	2.61	2.11	1.92	1.91	2.14	2.39	2.69	3.06
5	2.56	2.04	1.91	1.91	2.09	2.37	2.70	3.07
10	2.57	2.01	1.88	1.89	2.09	2.40	2.69	3.05
1000 K								
-10	2.40	2.02	1.86	1.89	2.18	2.49	2.71	3.03
-5	2.37	1.95	1.84	1.86	2.18	2.42	2.70	3.03
0	2.33	1.87	1.78	1.83	2.16	2.45	2.65	3.06
5	2.26	1.84	1.77	1.82	2.13	2.40	2.64	3.00
10	2.30	1.82	1.75	1.79	2.09	2.40	2.60	2.96
800 K								
-10	2.20	1.85	1.72	1.81	2.19	2.49	2.69	2.99
-5	2.18	1.73	1.72	1.80	2.17	2.45	2.66	3.00
0	2.18	1.72	1.68	1.76	2.14	2.41	2.61	2.99
5	2.16	1.67	1.61	1.72	2.14	2.38	2.60	2.95
10	2.09	1.61	1.61	1.72	2.12	2.36	2.57	2.92
600 K								
-10	2.03	1.69	1.67	1.76	2.18	2.41	2.61	2.96
-5	2.01	1.63	1.61	1.74	2.16	2.43	2.60	2.95
0	2.02	1.56	1.59	1.72	2.14	2.40	2.57	2.95
5	1.99	1.51	1.56	1.72	2.14	2.37	2.56	2.92
10	1.94	1.46	1.52	1.67	2.10	2.36	2.55	2.92

8.2. Defect Diffusion Coefficients

Table A3: Diffusion coefficients of interstitials fit to an Arrhenius function: $D = D_0 exp(-E_m/kT)$. E_m is in units of eV and D_0 is in units of cm^2/s.

Composition	-10 bar		-5 bar		0 bar		5 bar		10 bar	
	E_m	D_0	E_m	D_0	E_m	D_0	E_m	D_0	E_m	D_0
bcc U	0.122	3.001×10^{-4}	0.128	3.292×10^{-4}	0.125	3.160×10^{-4}	0.122	3.094×10^{-4}	0.121	3.075×10^{-4}
U-5Mo	0.221	6.087×10^{-4}	0.217	5.763×10^{-4}	0.223	6.048×10^{-4}	0.229	6.388×10^{-4}	0.233	6.576×10^{-4}
U-10Mo	0.317	1.161×10^{-3}	0.323	1.204×10^{-3}	0.326	1.197×10^{-3}	0.370	1.884×10^{-3}	0.337	1.249×10^{-3}
U-15Mo	0.434	2.792×10^{-3}	0.424	2.375×10^{-3}	0.443	2.727×10^{-3}	0.437	2.453×10^{-3}	0.483	3.908×10^{-3}
U-30Mo	0.582	5.778×10^{-3}	0.575	5.044×10^{-3}	0.614	6.963×10^{-3}	0.593	5.537×10^{-3}	0.607	6.266×10^{-3}
U-50Mo	0.758	1.824×10^{-2}	0.764	1.891×10^{-2}	0.747	1.576×10^{-2}	0.716	1.137×10^{-2}	0.773	1.786×10^{-2}
bcc Mo	0.275	7.616×10^{-4}	0.272	7.352×10^{-4}	0.273	7.426×10^{-4}	0.266	7.025×10^{-4}	0.264	6.857×10^{-4}

Table A4: Diffusion coefficients of vacancies fit to an Arrhenius function: $D = D_0 exp(-E_m/kT)$. E_m is in units of eV and D_0 is in units of cm^2/s.

Composition	-10 bar		-5 bar		0 bar		5 bar		10 bar	
	E_m	D_0	E_m	D_0	E_m	D_0	E_m	D_0	E_m	D_0
bcc U	0.502	4.390×10^{-3}	0.461	3.129×10^{-3}	0.420	2.150×10^{-3}	0.401	1.880×10^{-3}	0.381	1.596×10^{-3}
U-5Mo	0.598	7.794×10^{-3}	0.593	7.121×10^{-3}	0.590	6.906×10^{-3}	0.601	7.819×10^{-3}	0.607	8.209×10^{-3}
U-10Mo	0.753	1.933×10^{-2}	0.663	7.189×10^{-3}	0.692	9.702×10^{-3}	0.758	1.891×10^{-2}	0.661	6.375×10^{-3}
U-15Mo	0.803	1.675×10^{-2}	0.803	1.651×10^{-2}	0.752	9.540×10^{-3}	0.791	1.313×10^{-2}	0.821	1.831×10^{-2}
U-30Mo	0.906	1.541×10^{-2}	0.797	5.700×10^{-3}	0.843	8.797×10^{-3}	0.824	6.677×10^{-3}	0.836	7.553×10^{-3}
U-50Mo	0.904	8.768×10^{-3}	0.834	4.742×10^{-3}	0.894	7.550×10^{-3}	0.842	4.855×10^{-3}	0.894	8.043×10^{-3}
bcc Mo	1.265	2.665×10^{-2}	1.228	1.960×10^{-2}	1.428	1.133×10^{-1}	1.211	1.711×10^{-2}	1.204	1.620×10^{-2}

References

[1] K. Daum, C. Miller, B. Durtschi, and J. Cole. U-10mo monolithic fuel qualification plan. Technical Report INL/EXT-13-30238 rev2, Idaho National Laboratory, 2021.

[2] M. Meyer, J. Gan, J. Jue, D. Keiser, E. Perez, A. Robinson, D. Wachs, N. Woolstenhulme, G. Hofman, and Y. Kim. Irradiation performation of u-mo monolithic fuel. *Nucl. Eng. Tech.*, 46:169, 2014.

[3] HO JIN RYU and YEON SOO KIM. Influence of fuel-matrix interaction on the breakaway swelling of u-mo dispersion fuel in al. *Nuclear Engineering and Technology*, 46(2):159–168, 2014.

[4] A.B. Robinson, W.J. Williams, W.A. Hanson, B.H. Rabin, N.J. Lybeck, and M.K. Meyer. Swelling of u-mo monolithic fuel: Developing a predictive swelling correlation under research reactor conditions. *Journal of Nuclear Materials*, 544:152703, 2021.

[5] Charlyne Smith, Kaustubh Bawane, Daniele Salvato, Mukesh Bachhav, Dennis Keiser, Brandon Miller, Jian Gan, Jan-Fong Jue, Dong Choe, Paul Gilbreath, and William Hanson. Early self-organization of fission gas bubble superlattice formation in neutron-irradiated monolithic u-10mo fuels. *Journal of Nuclear Materials*, 578:154358, 2023.

[6] J. Gan, D.D. Keiser, B.D. Miller, A.B. Robinson, D.M. Wachs, and M.K. Meyer. Thermal stability of fission gas bubble superlattice in irradiated u–10mo fuel. *Journal of Nuclear Materials*, 464:1–5, 2015.

[7] Charlyne A. Smith, Sudipta Biswas, Brandon D. Miller, Boopathy Kombaiah, David Frazer, Dennis D. Keiser, and Assel Aitkaliyeva. High burnup structure formation in u-mo fuels. *Journal of Nuclear Materials*, 563:153617, 2022.

[8] Shenyang Hu and Benjamin Beeler. Gas bubble evolution in polycrystalline umo fuels under elastic-plastic deformation: A phase-field model with crystal-plasticity. *Frontiers in Materials*, 8, 2021.

[9] Xiaobin Jian, Feng Yan, Xiangzhe Kong, and Shurong Ding. Effects of u-mo irradiation creep coefficient on the mesoscale mechanical behavior in u-mo/al monolithic fuel plates. *Nuclear Materials and Energy*, 21:100706, 2019.

[10] Hakan Ozaltun, James I. Cole, and Barry H. Rabin. Thermomechanical Performance Assessment of U-Mo Monolithic Fuel Plates With Zircaloy Cladding. *Journal of Nuclear Engineering and Radiation Science*, 10(2):021601, 11 2023.

[11] Y. Kim, G. Hofman, J. Cheon, A. Robinson, and D. Wachs. Fission induced swelling and creep of U-Mo alloy fuel. *J. Nucl. Mater.*, 437:37, 2013.

[12] Xiaoxiao Mao, Xiaobin Jian, Jingyu Zhang, Feng Yan, Shurong Ding, Yongzhong Huo, Haoyu Wang, Lin Zhang, and Yuanming Li. Effects of u-mo irradiation creep performance on the thermo-mechanical coupling behavior in u-mo/al monolithic fuel assemblies. *Frontiers in Energy Research*, 9, 2021.

[13] B. Ye, G. Hofman, A. Leenaers, A. Bergeron, V. Kuzminov, S. Van den Berghe, Y.S. Kim, and H. Wallin. A modelling study of the inter-diffusion layer formation in U-Mo/Al dispersion fuel plates at high power. *J. Nucl. Mater.*, 499:191, 2018.

[14] S. Hu, V. Joshi, and C. Lavender. A rate-theory–phase-field model of irradiation-induced recrystallization in UMo nuclear fuels. *JOM*, 69:2554, 2017.

[15] S. L. Dudarev, M. R. Gilbert, K. Arakawa, H. Mori, Z. Yao, M. L. Jenkins, and P. M. Derlet. Langevin model for real-time brownian dynamics of interacting nanodefects in irradiated metals. *Phys. Rev. B*, 81:224107, Jun 2010.

[16] Bei Ye, Aaron Oaks, Shenyang Hu, Benjamin Beeler, Jeff Rest, Zhi-Gang Mei, and Abdellatif Yacout. Integrated simulation of u-10mo monolithic fuel swelling behavior. *Journal of Nuclear Materials*, 583:154542, 2023.

[17] Christoph Freysoldt, Blazej Grabowski, Tilmann Hickel, Jörg Neugebauer, Georg Kresse, Anderson Janotti, and Chris G. Van de Walle. First-principles calculations for point defects in solids. *Rev. Mod. Phys.*, 86:253–305, Mar 2014.

[18] D.J. Bacon, D.M. Barnett, and R.O. Scattergood. Anisotropic continuum theory of lattice defects. *Progress in Materials Science*, 23:51–262, 1980.

[19] Gyuchul Park, Benjamin Beeler, and Maria A. Okuniewski. An atomistic study of defect energetics and diffusion with respect to composition and temperature in γu and γu-mo alloys. *Journal of Nuclear Materials*, 552:152970, 2021.

[20] S.V. Starikov, L.N. Kolotova, A.Yu. Kuksin, D.E. Smirnova, and V.I. Tseplyaev. Atomistic simulation of cubic and tetragonal phases of u-mo alloy: Structure and thermodynamic properties. *Journal of Nuclear Materials*, 499:451 – 463, 2018.

[21] D. Smirnova, A. Kuksin, and S. Starikov. Investigation of point defects diffusion in bcc uranium and U-Mo alloys. *J. Nucl. Mater.*, 458:304, 2015.

[22] D. Smirnova, A. Kuksin, S. Starikov, and V. Stegailov. Atomistic modeling of the self-diffusion in gamma u and gamma u-mo. *Phys. Met. and Metall.*, 116:445, 2015.

[23] B. Beeler, Y. Zhang, ATM J. Hasan, G. Park, S. Hu, and Z.-G. Mei. Analyzing the effect of pressure on the properties of point defects in γu–mo through atomistic simulations. *MRS Advances*, 8:6, 2023.

[24] Elton Y. Chen, Chaitanya Deo, and Rémi Dingreville. Atomistic simulations of temperature and direction dependent threshold displacement energies in α- and γ-uranium. *Computational Materials Science*, 157:75–86, 2019.

[25] Benjamin Beeler, Yongfeng Zhang, Maria Okuniewski, and Chaitanya Deo. Calculation of the displacement energy of α and γ uranium. *Journal of Nuclear Materials*, 508:181–194, 2018.

[26] Yinbin Miao, Benjamin Beeler, Chaitanya Deo, Michael I. Baskes, Maria A. Okuniewski, and James F. Stubbins. Defect structures induced by high-energy displacement cascades in γ uranium. *Journal of Nuclear Materials*, 456:1–6, 2015.

[27] Sergey V. Starikov, Zeke Insepov, Jeffrey Rest, Alexey Yu. Kuksin, Genri E. Norman, Vladimir V. Stegailov, and Alexey V. Yanilkin. Radiation-induced damage and evolution of defects in mo. *Phys. Rev. B*, 84:104109, Sep 2011.

[28] Wenhong Ouyang, Wensheng Lai, Jiahao Li, Jianbo Liu, and Baixin Liu. Atomic simulations of u-mo under irradiation: A new angular dependent potential. *Metals*, 11(7), 2021.

[29] Xiao-Feng Tian, Hong-Xing Xiao, Rui Tang, and Chun-Hai Lu. Molecular dynamics simulation of displacement cascades in u–mo alloys. *Nuclear Instruments and Methods in Physics Research Section B: Beam Interactions with Materials and Atoms*, 321:24–29, 2014.

[30] L.N. Kolotova and S.V. Starikov. Atomistic simulation of defect formation and structure transitions in u-mo alloys in swift heavy ion irradiation. *Journal of Nuclear Materials*, 495:111–117, 2017.

[31] Shenyang Hu, Wahyu Setyawan, Benjamin W. Beeler, Jian Gan, and Douglas E Burkes. Defect cluster and nonequilibrium gas bubble associated growth in irradiated umo fuels – a cluster dynamics and phase field model. *Journal of Nuclear Materials*, 542:152441, 2020.

[32] F Gao, D.J Bacon, P.E.J Flewitt, and T.A Lewis. The influence of strain on defect generation by displacement cascades in α-iron. *Nuclear Instruments and Methods in Physics Research Section B: Beam Interactions with Materials and Atoms*, 180(1):187–193, 2001. Computer Simulation of Radiation Effects in Solids.

[33] S. Miyashiro, S. Fujita, and T. Okita. Md simulations to evaluate the influence of applied normal stress or deformation on defect production rate and size distribution of clusters in cascade process for pure cu. *Journal of Nuclear Materials*, 415(1):1–4, 2011.

27

[34] B. Beeler, M. Asta, P. Hosemann, and N. Gronbech-Jensen. Effects of applied strain on radiation damage generation in body-centered cubic iron. *J. Nucl. Mater.*, 459:159, 2015.

[35] M. Abu-Shams and I. Shabib. Primary radiation damage of fe-10%cr models under uniaxial, biaxial, and hydrostatic pressure using md simulation. *Journal of Nuclear Materials*, 509:335–342, 2018.

[36] S. Plimpton. Fast parallel algorithms for short-range molecular dynamics. *J. Comp. Phys.*, 117:1–19, 1995.

[37] A. P. Thompson, H. M. Aktulga, R. Berger, D. S. Bolintineanu, W. M. Brown, P. S. Crozier, P. J. in 't Veld, A. Kohlmeyer, S. G. Moore, T. D. Nguyen, R. Shan, M. J. Stevens, J. Tranchida, C. Trott, and S. J. Plimpton. LAMMPS - a flexible simulation tool for particle-based materials modeling at the atomic, meso, and continuum scales. *Comp. Phys. Comm.*, 271:108171, 2022.

[38] Benjamin Beeler and Yongfeng Zhang. The reconciliation and validation of a combined interatomic potential for the description of xe in γu-mo. *Frontiers in Nuclear Engineering*, 2, 2023.

[39] Gyuchul Park, Benjamin Beeler, and Maria A. Okuniewski. Computational determination of a primary diffusion mode in γu-10mo under irradiation. *Journal of Nuclear Materials*, 574:154137, 2023.

[40] Yuhao Wang, Benjamin Beeler, and Andrea Jokisaari. An atomistic study of fundamental bulk and defect properties in α-uranium. *Journal of Nuclear Materials*, 576:154289, 2023.

[41] Khadija Mahbuba, Benjamin Beeler, and Andrea Jokisaari. Grain boundary self-diffusion and point defect interactions in α-u via molecular dynamics. *Journal of Nuclear Materials*, 604:155521, 2025.

[42] ATM Jahid Hasan and Benjamin Beeler. Calculation of grain boundary diffusion coefficients in γu-mo using atomistic simulations. *Journal of Nuclear Materials*, 598:155190, 2024.

[43] S. Starikov and D. Smirnova. Details of structure transformations in pure uranium and u-mo alloys: Insights from classical atomistic simulation. *Journal of Nuclear Materials*, 576:154265, 2023.

[44] Lada Kolotova and Ilia Gordeev. Structure and phase transition features of monoclinic and tetragonal phases in u–mo alloys. *Crystals*, 10(6), 2020.

[45] D. Chaney, A. Castellano, A. Bosak, J. Bouchet, F. Bottin, B. Dorado, L. Paolasini, S. Rennie, C. Bell, R. Springell, and G. H. Lander. Tuneable correlated disorder in alloys. *Phys. Rev. Mater.*, 5:035004, Mar 2021.

[46] P. Soderling, B. Grabowski, L. Yang, A. Landa, T. Bjorkman, P. Souvatis, and O. Eriksson. High-temperature phonon stabilization of ! -uranium from relativistic first-principles theory. *Phys. Rev. B*, 85:060301, 2012.

[47] M. Meyer, G. Hofman, S. Hayes, C. Clark, T. Wiencek, J. Snelgrove, R. Strain, and K. Kim. Low-temperature irradiation behavior of uranium-molybdenum alloy dispersion fuel. *J. Nucl. Mater.*, 304:221, 2002.

[48] Yongfeng Zhang, Anus Manzoor, Chao Jiang, Dilpuneet Aidhy, and Daniel Schwen. A statistical approach for atomistic calculations of vacancy formation energy and chemical potentials in concentrated solid-solution alloys. *Computational Materials Science*, 190:110308, 2021.

[49] Miaomiao Jin, Yipeng Gao, Chao Jiang, and Jian Gan. Defect dynamics in γ-u, mo, and their alloys. *Journal of Nuclear Materials*, 549:152893, 2021.

[50] Yaakov Kraftmakher. Equilibrium vacancies and thermophysical properties of metals. *Physics Reports*, 299(2):79–188, 1998.

[51] C. Varvenne and E. Clouet. Elastic dipoles of point defects from atomistic simulations. *Physical Review B*, 96:224103, 2017.

[52] J. Ziegler, J. Biersack, and U. Littmark. *Stopping and Ranges of Ions in Matter.* Pergamon Press, 1985.

[53] Lin-Chieh Yu, Shuxiang Zhou, Miaomiao Jin, Marat Khafizov, David Hurley, and Yongfeng Zhang. Establishing the temperature and orientation dependence of the threshold displacement energy in tho2 via molecular dynamics simulations. *Nuclear Materials and Energy*, 41:101774, 2024.

[54] Xinwei Wang, Mengxin Yang, Xiaoqian Gai, Yibo Sun, Bohan Cao, Jiajin Chen, Min Liang, Fubo Tian, and Liang Li. A comprehensive investigation on the accuracy and efficiency of methods for melting temperature calculation using molecular dynamics simulations. *Journal of Molecular Liquids*, 395:123924, 2024.

[55] YangChun Zou, ShiKai Xiang, and ChengDa Dai. Investigation on the efficiency and accuracy of methods for calculating melting temperature by molecular dynamics simulation. *Computational Materials Science*, 171:109156, 2020.

[56] H. Okamoto. Mo-u (molybdenum-uranium). *Journal of Phase Equilibria and Diffusion*, 33(6):497–497, 2012.

[57] B. Beeler, M. Asta, P. Hosemann, and N. Gronbech-Jensen. Effect of strain and temperature on the threshold displacement energy in body-centered cubic iron. *J. Nucl. Mater.*, 474:113, 2016.

[58] B. Beeler, B. Good, S. Rashkeev, C. Deo, M. Baskes, and M. Okuniewski. First principles calculations for defects in U. *J. Phys.: Cond. Mat.*, 22:505703, 2010.

[59] Francois Willaime and Carlo Massobrio. A molecular dynamics study of zirconium based on an n-body potential: Hcp/bcc phase transformation and diffusion mechanisms in the bcc-phase. *MRS Online Proceedings Library*, 193(1):295–300, 1990.

[60] M. Meyer, B. Rabin, J. Cole, I. Glagolenko, W. Jones, J-F. Jue, Jr. D. Keiser, C. Miller, G. Moore, H. Ozaltun, F. Rice, A. Robinson, J. Smith, D. Wachs, W. Williams, and N. Woolstenhulme. Preliminary report on U-Mo monolithic fuel for research reactors. Technical Report INL/EXT-17-40975, Idaho National Laboratory, 2017.

[61] M. Norgett, M. Robinson, and L. Torrens. A proposed method of calculating displacement dose rates. *Nucl. Eng. Design*, 33:50–54, 1975.

[62] G H Kinchin and R S Pease. The displacement of atoms in solids by radiation. *Reports on Progress in Physics*, 18(1):1, jan 1955.

[63] K. Nordlund, S. Zinkle, A. Sand, F. Granberg, R. Averback, R. Stoller, T. Suzudo, L. Malerba, F. Banhart, W. Weber, F. Willaime, S. Dudarev, and D. Simeone. mproving atomic displacement and replacement calculations with physically realistic damage models. *Nature Communications*, 9:1084, 2018.